Perivascular pumping in the mouse brain: Realistic boundary conditions reconcile theory, simulation, and experiment

Antonio Ladrón-de-Guevara[a,b], **Jessica K. Shang**[c], **Maiken Nedergaard**[a,d,e], **and Douglas H. Kelley**[c,e,1]

[a]Center for Translational Neuromedicine, University of Rochester Medical Center, Rochester, NY, 14627, USA; [b]Department of Biomedical Engineering, University of Rochester, Rochester, NY, 14627, USA; [c]Department of Mechanical Engineering, University of Rochester, Rochester, NY, 14627, USA; [d]Department of Neuroscience, University of Rochester, Rochester, NY, 14627, USA; [e]Center for Translational Neuromedicine, University of Copenhagen, 2100 Copenhagen, Denmark

This manuscript was compiled on July 2, 2020

Cerebrospinal fluid (CSF) flows through the perivascular spaces surrounding cerebral arteries. Revealing the mechanisms driving its flow would bring improved understanding of brain waste transport and insights for disorders including Alzheimer's disease, stroke, and traumatic brain injury. In vivo CSF velocity measurements in mice have been used to argue that flow is driven primarily by the pulsatile motion of artery walls — perivascular pumping. However, fluid dynamics theory and simulation have predicted that perivascular pumping produces flows differing from in vivo observations starkly, particularly in the phase and relative amplitude of flow oscillation. Here we show that coupling theoretical and simulated flows to realistic end boundary conditions, using resistance and compliance values measured in mice, results in velocities that match observations closely in phase, relative amplitude of oscillation, and mean flow speed. This new, quantitative agreement among theory, simulation, and in vivo measurement further supports the idea that perivascular pumping is a primary CSF driver in physiological conditions.

cerebrospinal fluid, glymphatic system, brain, perivascular pumping, compliance, hydraulic resistance

Cerebrospinal fluid (CSF) flows throughout the skull, and its motion plays an important role in the mass transport. A brain-wide fluid pathway, the glymphatic system (1), has been proposed to bring flowing fluid close to much or all of the brain parenchyma, enabling waste evacuation and nutrient/neurotransmitter delivery at rates more rapid than would be possible with diffusion alone, and acting almost exclusively during sleep. In vivo observations in mice (2) and rats (3, 4) have shown brain-wide mass transport consistent with that proposal. CSF flow has been observed to vary with electrophysiological activity in the brain (5) and to play a key role in stroke (6). CSF likely exits the skull via several routes, including uptake at the arachnoid villi and efflux via lymph vessels (7–9).

CSF has long been known to flow in the perivascular spaces (PVSs) that surround arteries in the brain (10, 11). Real-time in vivo imaging has provided strong evidence that CSF in PVSs pulses in synchrony with the cardiac cycle and has mean flow direction parallel, not antiparallel, to the blood flow (12, 13). Though some papers argue that the mean flow proceeds in the opposite direction (13–15) and through basement membranes in the artery wall, fixation artifacts may undermine post-mortem tracer distribution as an indicator of flow (12, 16). A recent review (17) summarizes current knowledge of mass transport in brain tissue.

Pulsation in synchrony with the cardiac cycle suggests a causal link between CSF flow in PVSs and blood flow. Hadaczek et al. (18) proposed that the dilations and constrictions traveling along artery walls with each heart beat might drive CSF in the same direction, in a peristalsis-like mechanism they dubbed "perivascular pumping." As evidence, they presented experimental results showing that macromolecules injected into the central nervous systems of rats were transported further in animals with beating hearts than in animals whose hearts had recently been stopped. Iliff et al. (19) presented additional evidence in support of the hypothesis. Peristalsis is known to occur in other parts of the body, including the urethra and digestive system (20). More recent theoretical (14, 21) and numerical (22–24) studies have indeed shown that net fluid motion is possible (except when dilations and constrictions do not travel (25)).

CSF flow is linked to blood flow via another mechanism as well. Consistent with the conservation of mass (sometimes called the Monro-Kellie doctrine in this context), blood entry into the rigid skull must be accompanied by CSF exit, and vice-versa. Though local regions are more flexible than the skull, expansion of blood vessels often implies reduction of nearby PVS volumes. Local variation of blood flow with metabolic demand (functional hyperemia) affects CSF flow (26), causes important coupling to electrophysiological activity (5) and drives pathological CSF flow during stroke (6). It is a promis-

Significance Statement

The brain is immersed in cerebrospinal fluid, whose flow has long been thought to remove metabolic wastes and transport neurotransmitters, in addition to offering a potential path for drug delivery. Fluid has been hypothesized to enter the deep brain along spaces that surround arteries, but the mechanisms driving flow there have been debated. Experiments suggest artery wall pulsation drives the fluid in healthy conditions, but theories and simulations have predicted that wall-driven flows would have stronger oscillations and different phase than what is observed. We show that coupling those predictions to a simple but realistic model of the rest of the fluid pathway reconciles the differences, so that theory, simulation, and experiment agree.

ALGR carried out the laboratory experiments and analyzed the resulting data. JKS carried out the simulations and analyzed the resulting data. MN participated in the design of the study and revised the manuscript. DHK conceived of the study, designed the study, and drafted the manuscript. All authors gave final approval for publication and agree to be held accountable for the work performed therein.

The authors declare no conflicts of interest.

[1]To whom correspondence should be addressed. E-mail: d.h.kelley@rochester.edu

ing topic for further study which we will leave for future work.

Perivascular pumping has been studied analytically (see (27) for a recent review), but the flows predicted using reasonable approximations and realistic parameters differ starkly from in vivo observations. Schley et al. (14) produced an analytic prediction of the flow due to perivascular pumping in an open, two-dimensional, Cartesian space, based on the lubrication approximation and rigorous in the case of long wavelengths. For sinusoidal dilations and constrictions with a $b = 0.3$ μm half-amplitude traveling at $c = 1$ m/s on one wall of a channel with width $H = 40$ μm, their theory predicts a flow in which the mean downstream velocity is 0.034 μm/s. Later in vivo measurements found a mean downstream velocity of 18.7 μm/s (12). Allowing for uncertainty in the input parameters and for the analytic simplifications involved, particularly the geometric differences between a two-dimensional Cartesian space and a three-dimensional annular space, the prediction and observations seem to agree reasonably well. Analysis and observations disagree, however, on the phase and relative amplitude of oscillation. Flow oscillation is predicted to lag the wall velocity (which we define as the rate of PVS channel constriction, consistent with (12)) by $\varphi = 270^\circ$, but in vivo observations indicate flow oscillations lag wall velocity by $\varphi = 353^\circ$. The ratio of oscillatory to steady amplitude predicted analytically is $\gamma = 22,200$, but in observations, dividing the peak root-mean-square velocity oscillation by the mean downstream velocity yields $\gamma = 0.53$. Thus if the mean flow were the same, oscillations in observed flows would need to be about 40,000 times faster in order to match the prediction.

Wang and Olbricht (21), also using lubrication theory and the long-wavelength approximation, produced an analytic prediction of the flow due to perivascular pumping in a cylindrical annulus filled with a porous medium. For sinusoidal dilations and constrictions with the same 0.3 μm half-amplitude and the same speed 1 m/s, traveling on the inner wall of an annulus with inner radius $r_1 = 30$ μm and outer radius $r_2 = 70$ μm, with porosity $\varepsilon = 1$, their theory predicts a flow with mean downstream velocity 10.13 μm/s, quite close to the 18.7 μm/s observed value. But disagreement again arises on oscillation phase and amplitude. Like Schley et al. (14), Wang and Olbricht predict a $\varphi = 270^\circ$ phase lag from wall velocity to flow oscillations, disagreeing with observations. The Wang and Olbricht theory predicts $\gamma = 443$, far from $\gamma = 0.53$, as observed in vivo.

Perivascular pumping has also been studied using numerical simulations, which likewise predicted flows that differ starkly from in vivo observations. Kedarasetti et al. (24) recently performed a series of simulations. The first set considered axisymmetric flows in an open (not porous) cylindrical annulus with inner radius 30 μm and outer radius 70 μm. Sinusoidal dilations and constrictions with half-amplitude on the order of 0.3 μm, speed 1 m/s, and frequency 8.67 Hz propagated on the inner wall. The computational domain was one wavelength long, with periodic end boundaries. Though the authors did not report the mean flow speed or volume flow rate, they did state that for realistic speeds, the phase of flow oscillations lagged wall velocity by $\varphi = 270^\circ$, agreeing with predictions from lubrication theory (14, 21) but not with in vivo observations (12). The authors also stated that $\gamma \sim 100$, again disagreeing with in vivo observations.

The second set of simulations by Kedarasetti et al. (24) considered flow in a three-dimensional domain whose cross-sectional size and shape are similar to in vivo observations (1, 12, 13) and similar to annular shapes that have minimum hydraulic resistance (28). Essentially, the domain lay between a circular artery and an elliptical outer wall. Dilations and constrictions on the inner wall propagated at $c = 1$ m/s with frequency $f = 8.67$ Hz but were not sinusoidal; rather, their shape and amplitude were taken from the in vivo observations of Mestre, Tithof, et al. (12). The pressure was set to zero at the end boundaries. The simulations predicted a time-averaged centerline velocity of 102.1 μm/s, in reasonable agreement with the 18.7 μm/s observed in vivo. The phase difference between wall velocity and flow oscillations is not stated, but judging from Fig. 3c in (24), flow oscillations lag wall velocity by $\varphi \approx 330^\circ$, significantly different from zero. And the ratio of oscillations to steady flow was $\gamma = 290$, strikingly different than $\gamma = 0.53$ as observed in vivo. Kedarasetti et al. (24) also presented a third set of simulations, to be discussed below.

Repeatedly, analytic and numerical predictions of the mean flow caused by perivascular pumping agree reasonably well (if not perfectly) with each other and with mean flows observed in vivo. Analytic and numerical predictions agree that flow oscillations lag wall velocity by a substantial phase difference (270° to 330°), but in vivo observations indicate nearly zero phase difference. And when considering the relative amplitude of oscillation γ, though the values vary, theory and simulations have consistently predicted that perivascular pumping would drive far stronger oscillations than have been observed in vivo.

One explanation might be that perivascular pumping is not a primary driver of flows observed in vivo, as Kedarasetti et al. (24) and others (23, 29–31) have argued. CSF production by choroid plexus and uptake by arachnoid villi likely drive some flow. Other osmotic processes might be at play. Non-physiological flow induced by injection of tracer particles has been offered as an explanation (24, 30–34), though Mestre, Tithof et al. (6) measured flow speeds that had insignificant dependence on whether injection was in progress, and insignificant decay after injection ceased. Those authors also demonstrated that altering the artery wall motion substantially changed CSF flow characteristics and significantly reduced the mean flow speed. Thus perivascular pumping is likely to play some role. An explanation of the discrepancies among theory, simulation, and experimental observation is badly needed.

Here we present evidence that the discrepancies originate from — and can be resolved with — the end boundary conditions. The flow produced by a perivascular pump depends on the pathways coupled to the pump, into which the pumped fluid must pass. Those pathways can be characterized with simple but realistic lumped parameters: hydraulic resistance and compliance. We present in vivo measurements of those parameters, then demonstrate that coupling existing analytic and numerical perivascular pumping models to a lumped-parameter pathway model produces flows that closely match in vivo observations.

1. Lumped-parameter model for boundary conditions

The stunning intricacy of the brain makes it impossible to study the global CSF pathway in full detail. Some mechanisms are unknown, some processes occur at length and time scales unmeasurable with current technology, and a full numerical

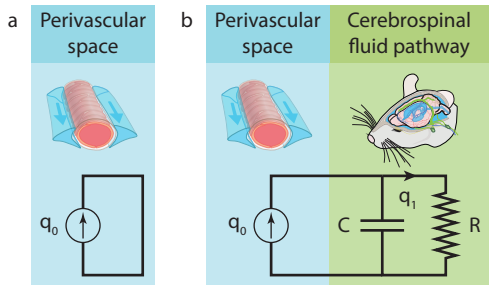

Fig. 1. (a), A lumped-parameter characterization of perivascular pumping, uncoupled from other fluid pathways. (b), A lumped-parameter characterization of perivascular pumping coupled to other fluid pathways.

simulation would overwhelm supercomputers. Thus it is practical to separate the CSF pathway into components that can be considered separately. Perivascular pumping in a PVS is most simply represented as a source that produces an average volume flow rate q_0. Considered in isolation, it can be represented by the closed-loop fluid pathway sketched in Fig. 1a. This uncoupled pathway is the lumped-parameter representation of perivascular pumping as considered by all past theoretical and computational studies, including those described above. Periodic end boundary conditions, zero-pressure boundary conditions, and infinite domains are equivalent, in the lumped-parameter characterization, to making a direct connection between the PVS inlet and outlet.

Realistic modeling, however, requires accounting for interactions when components are connected. To understand how a peristaltic pump interacts with the rest of the CSF pathway, additional lumped parameters must be introduced, as sketched in Fig. 1b. We will characterize the rest of the CSF pathway using a compliance C, which accounts for elasticity of tissues that bound CSF spaces, and a resistance R. The hydraulic resistance of a component or pathway characterizes the difficulty of CSF passing, is analogous to electrical resistance, and is defined as the pressure difference across the component (or pathway) divided by the volume flow rate through it. More complex lumped-parameter characterizations are possible, but this one is sufficient for the discussion at hand. In particular, including both a compliance and a resistance is essential because we are interested in pulsatile flows and need to account for the characteristic timescale of the CSF pathway: RC. (Some studies discuss the same mechanics in terms of the elastance C^{-1}.)

With components modeled as in Fig. 1b, conservation of mass and energy together require that the volume flow rate q_1 through the rest of the CSF pathway satisfy

$$\frac{\partial q_1}{\partial t} + \frac{q_1}{RC} = \frac{q_0}{RC}. \qquad [1]$$

Lumped-parameter characterizations of perivascular pumping and of the rest of the CSF pathway make it possible to predict the flow in the *coupled* system from the flow in the uncoupled system, if the resistance R and compliance C can be determined.

To characterize the resistance and compliance of the CSF pathway, we performed bolus-injection experiments in 7 mice, as described in Methods, using the setup shown in Fig. 2. The resulting variation of ICP over time is shown in Fig. 3. From an average value $P_0 = 2.830 \pm 0.381$ mmHg before injection, the ICP increased suddenly to a maximum value $P_{\max}$, then decayed gradually. The decay was nearly exponential, as we would expect from a linear RC system. We calculated the compliance C from the pressure-volume index (PVI), as described in Methods. The resulting R and C values for $N = 7$ mice are shown in Fig. 3. The resistance is $R = (8.772 \pm 0.722) \times 10^{12}$ Pa·s/m^3 $= 1.097 \pm 0.090$ mmHg/(μL/min) (mean $\pm$ standard error of the mean). The compliance is $C = (1.349 \pm 0.139) \times 10^{-11}$ m^3/Pa $= 1.798 \pm 0.185$ μL/mmHg. The corresponding time constant is $RC = 118.3$ s.

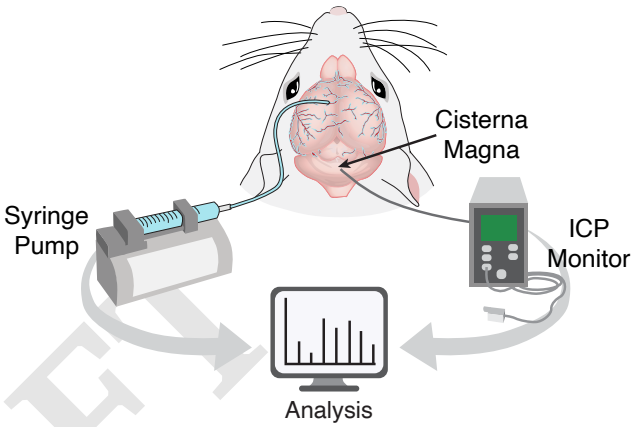

Fig. 2. Experimental setup. Injecting artificial CSF into the brain of an anesthetized mouse, we measure the resulting intracranial pressure (ICP) to determine the resistance and elastance of brain CSF spaces.

Other studies have determined the resistance and compliance of the CSF pathway. Jones (35) used a constant-rate infusion technique to measure the resistance of CSF spaces during development in normal and hydrocephalus mice. The author measured a resistance of 1.88±0.37 mmHg/(μL/min) in 5-week-old mice, in good agreement with the R value reported here. The marginally higher value reported by Jones (35) may be due to the infusion method. The bolus injection method is known to underestimate the resistance derived by the constant-rate infusion method (36, 37). We also measured the resistance using the constant-rate infusion method and obtained a value of $R = 1.927 \pm 0.315$ mmHg/(μL/min) which closely matches the value reported by Jones (35). Oshio et al. (38) measured a resistance of 5.149±1.103 mmHg/(μL/min) in CD-1 wild-type mice using a similar constant-rate infusion method. This higher resistance also explains their elevated resting ICP (6.988±1.030 mmHg) as compared to other studies with lower ICP levels ($\approx$ 4 mmHg) (39–41). This overestimation of the resistance and resting ICP may be due to the high pressure gradient established by the authors while the pipette was in the brain parenchyma to assess ventricle puncture ($\approx$ 29 mmHg). In another study from the same group, Papadopoulos et al. (42) measured the PVI in CD-1 wild-type mice using the bolus injection method. They reported a value of PVI $\approx$ 19 μL, higher than the values measured here (PVI $\approx$ 10 μL). However, based on their resting ICP, their compliance would be $C = 1.12$ μL/mmHg. This is in the range of our C value but smaller which agrees with exponential behavior of the CSF volume-pressure curve and a higher resting ICP (43).

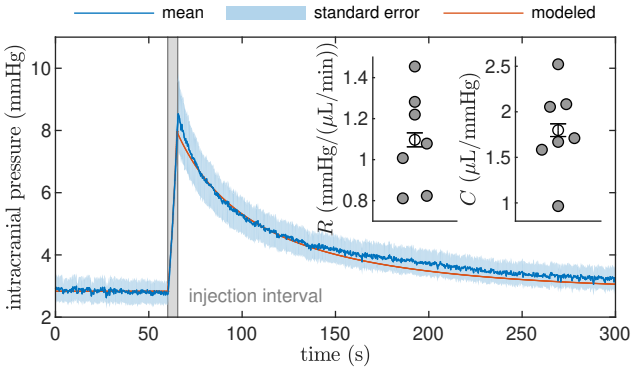

Fig. 3. Resistance and compliance of the cerebrospinal fluid pathway in mice, measured in vivo. After a brief and rapid fluid injection (1 μL/s for 5 s), intracranial pressure decays with dynamics well-modeled by an RC boundary condition, as sketched in Fig. 1. From pressure variations measured in $N = 7$ animals we calculate resistance $R = 1.097 \pm 0.090$ mmHg/(μL/min) and compliance $C = 1.798 \pm 0.185$ μL/mmHg.

2. Theoretical predictions with realistic end boundary conditions

Having characterized the perivascular pump and the CSF pathway in terms of the parameters R and C, we can now use Eq. 1 to determine the flow rate q_1 in the coupled system if the uncoupled flow rate q_0 is known. We will first determine q_1 from two analytic predictions of q_0.

Schley et al. (14) considered a two-dimensional Cartesian domain in which one wall dilates and constricts such that the channel width varies over time and space. Here we consider the general case of sinusoidal wall motion that follows $h = \mathcal{R}\left\{H + i\,b\,e^{i2\pi f(\frac{x}{c}-t)}\right\}$, where H is the mean channel width, b is the half-amplitude of dilation and constriction, c is the wave speed, x is the streamwise spatial coordinate, and $\mathcal{R}\{\cdot\}$ denotes the real part. Henceforth, whenever complex quantities appear, we consider only their real part, dropping the $\mathcal{R}\{\cdot\}$ notation. Applying lubrication theory and considering the long-wavelength case, Schley et al. found that perivascular pumping in the uncoupled system produces flow rate $\hat{q}_0 = c(h - h_0)$, where $h_0 = \overline{h^{-2}}/\overline{h^{-3}}$. From this expression, the quantities tabulated above can be calculated directly. The mean downstream velocity is $\overline{\hat{q}_0}/H = 0.034$ μm/s. The ratio of the amplitude of the oscillatory component to the amplitude of the steady component is $\gamma = b/(H - h_0) = 22,200$. The phase of the oscillatory component of $\hat{q}_0$ is identical to the phase of h and therefore lags the wall velocity $-\partial h/\partial t$ by $\varphi = 270°$.

Because the system is two-dimensional, $\hat{q}_0$ is an area (not volume) flow rate and Eq. 1 becomes

$$\frac{\partial \hat{q}_1}{\partial t} + \frac{\hat{q}_1}{\hat{R}\hat{C}} = \frac{\hat{q}_0}{\hat{R}\hat{C}}, \qquad [2]$$

where $\hat{q}_1$ is the area flow rate in the coupled system, $\hat{R} = Rw$, $\hat{C} = C/w$, and w is the width of the channel in the third dimension. Since w was not part of the original theory, we must choose it. Imagining extending the two-dimensional domain to produce a rectangular channel, we match its cross-sectional area to that of the annular channel considered in (24): $w = \pi(r_2^2 - r_1^2)/H = 94$ μm. The solution to Eq. 2 is

$$\hat{q}_1 = c(H - h_0) - \frac{bc}{2\pi f\hat{R}\hat{C} + i} e^{i2\pi f(\frac{x}{c}-t)} + \hat{q}_2 e^{-\frac{t}{\hat{R}\hat{C}}}. \qquad [3]$$

The last term is a starting transient that decays over time. Focusing our attention on fully-developed dynamics, we choose the integration constant $\hat{q}_2 = 0$. The wall velocity $\partial h/\partial t$, the uncoupled flow rate $\hat{q}_0$, and the coupled flow rate $\hat{q}_1$ are shown in Fig. 4.

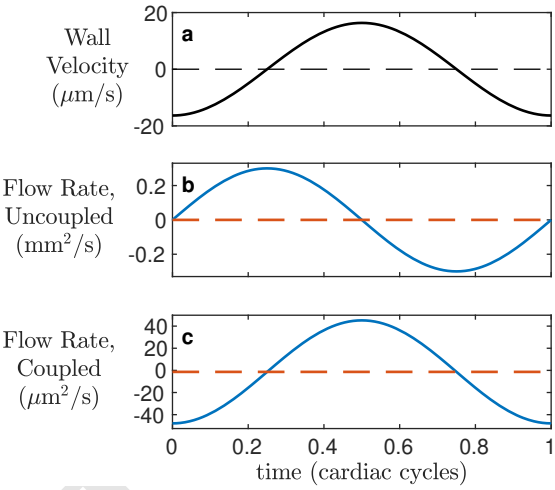

Fig. 4. Realistic boundary conditions alter the phase and relative amplitude of flow pulsations in the Schley et al. (14) solution for peristaltic pumping. (a), Artery wall velocity at $x = 0$, over one cycle. (b), Flow rate $\hat{q}_0$ when the peristaltic pump is uncoupled from the CSF pathway, at $x = 0$, over one cycle. (c), Flow rate $\hat{q}_1$ when the pump is coupled to the CSF pathway, at $x = 0$, over one cycle. Note that different units are used in panels (b) and (c). The phase and relative amplitude of flow oscillation agree closely with in vivo observations when coupled, but not when uncoupled.

The first term in Eq. 3 gives the steady component of the flow, unchanged from the uncoupled case, and still in reasonable agreement with the in vivo observations, given the approximations involved in this theory. The second term gives the oscillatory component, which lags the wall velocity $-\partial h/\partial t = 2\pi f b e^{i2\pi f(x/c-t)}$ by $\varphi = \arg(-bc(2\pi f\hat{R}\hat{C} + i)^{-1} - \arg 2\pi f b = \arctan(-2\pi f\hat{R}\hat{C})^{-1} - 0 = 0$. Coupling the perivascular pump to the rest of the CSF pathway shifts the phase of oscillation by 90°, so that the flow oscillates at nearly the same phase as the wall velocity. That phase shift is consistent with our expectations from the lumped-parameter model shown in Fig. 1: the CSF pathway acts like a first-order lowpass filter with cutoff frequency $(\hat{R}\hat{C})^{-1}$. Since $f \gg (\hat{R}\hat{C})^{-1}$, the phase shift imposed by the filter is well-approximated by $\arctan 2\pi f\hat{R}\hat{C} = 89.96°$. Because of that shift, the analytic solution of (14), when coupled to the rest of the CSF pathway, predicts that wall velocity and flow oscillations will have nearly the same phase, as observed in vivo.

The ratio of the amplitudes of the oscillatory and steady terms in Eq. 3 is $\gamma = b(H - h_0)^{-1}(4\pi^2\hat{R}^2\hat{C}^2f^2 + 1)^{-1/2} = 34.5$. Coupling the perivascular pump to the rest of the CSF pathway decreases γ by a factor of more than 600. That decrease is consistent with our expectations from the lumped-parameter model shown in Fig. 1. Since $f \gg (\hat{R}\hat{C})^{-1}$, the gain of the lowpass filter at frequency f is well-approximated by $(1+2\pi f\hat{R}\hat{C})^{-1} = 1.551 \times 10^{-4} = 1/645$. Without coupling, $\gamma = 22,200$, disagreeing by many orders of magnitude with $\gamma = 0.53$ measured in vivo. Coupling the analytic prediction of (14) to the rest of the CSF pathway, however, brings much closer agreement to in vivo observations, especially considering

that the theory is two-dimensional and Cartesian.

Wang and Olbricht (21) considered a porous, axisymmetric cylindrical annulus in which the inner wall dilates and constricts such that the channel width (distance between inner and outer walls) varies over time according to $h = r_2 - r_1 + i\,b\,e^{i2\pi f(\frac{x}{c}-t)}$. Applying lubrication theory and considering the long-wavelength case, they found that perivascular pumping in the uncoupled system and in the absence of other pressure gradients produces flow rate $q_0 = -2\pi\varepsilon c r_2^2/(\alpha_- + \alpha_+) + \pi\varepsilon c(r_2^2 - h^2)$, where ε is the porosity of the space, which we presume to be open ($\varepsilon = 1$), and $\alpha_\pm = ((1 \pm r_1/r_2)^2 - (b/r_2)^2)^{-1/2}$. From these expressions, the quantities tabulated above can be calculated directly. The mean downstream velocity is $\overline{q_0}/\pi/(r_2^2 - r_1^2) = 10.13$ μm/s. The ratio of the amplitude of the oscillatory component to the steady component is $\gamma = 443$. The phase of the oscillatory component of q_0 is identical to the phase of h and therefore lags the wall velocity $-\partial h/\partial t$ by $\varphi = 270°$.

Using Eq. 1, we can solve for q_1. The result is plotted in Fig. 5, along with the wall velocity $-\partial h/\partial t$ and the uncoupled flow rate q_0. (The analytic form of q_1 is lengthy, so we do not repeat it here.) Again, we neglect the transient term, and the mean downstream velocity is not changed by coupling the perivascular pump to the rest of the CSF pathway. The oscillatory component of q_1 lags the wall velocity $\partial h/\partial t$ by $\varphi = 359.9°$, agreeing well with in vivo observations. The ratio of the amplitude of the oscillatory component to the steady component is $\gamma = 0.069$, agreeing well with $\gamma = 0.53$ observed in vivo.

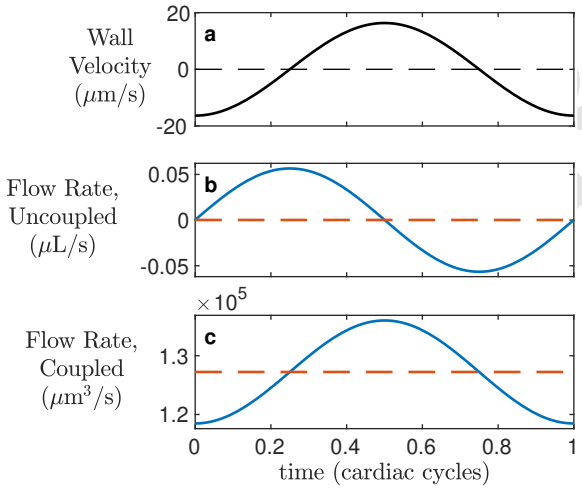

Fig. 5. Realistic boundary conditions alter the phase and relative amplitude of flow pulsations in the Wang and Olbricht (21) solution for peristaltic pumping. (a), Artery wall velocity over one cycle. (b), Flow rate $\hat{q}_0$ when the peristaltic pump is uncoupled from the CSF pathway, at $x = 0$, over one cycle. (c), Flow rate $\hat{q}_1$ when the pump is coupled to the CSF pathway, at $x = 0$, over one cycle. Note that different units are used in panels (b) and (c). The phase and relative amplitude of flow oscillation agree closely with in vivo observations when coupled, but not when uncoupled.

3. Simulation predictions with realistic end boundary conditions

Having demonstrated the effects of realistic end boundary conditions on two existing theoretical predictions, we now demonstrate the effect on existing predictions from simulation. As described above, the second set of simulations presented by Kedarasetti et al. (24) considered flow in a three-dimensional domain whose cross-sectional shape and size are similar to in vivo observations. The inner wall was made to dilate and constrict according to wall velocity measured in vivo (12); the wall velocity is plotted in Fig. 6a. The pressure was set to zero at end boundaries, again with the system isolated from the rest of the CSF pathway. Perivascular pumping produced the centerline velocity shown in Fig. 6b. As mentioned above, the time-averaged centerline velocity was 102.1 μm/s, the flow oscillations lag wall velocity by $\varphi \approx 330°$, and the ratio of oscillations to steady flow was $\gamma = 290$.

The cross-sectional mean velocity is not given in (24), but it is surely similar to the centerline velocity, perhaps smaller by 20-40%. Approximating the mean velocity as the centerline velocity, we can use the data shown in Fig. 6b to solve Eq. 1 numerically with a simple forward-Euler scheme. The cross-sectional area that relates mean velocities to volume flow rates is arbitrary, being the same for both q_0 and q_1. The result, shown in Fig. 6c, shows the centerline velocity predicted by the Kedarasetti et al. (24) simulation with realistic end boundary conditions, accounting for coupling to the rest of the CSF pathway. The time-averaged centerline velocity is 102.1 μm/s, in good agreement with the 18.7 μm/s observed in vivo. The peak of the centerline velocity lags the peak of the wall velocity by $\varphi = 356°$, similar to the in vivo observations. The ratio of the amplitude of oscillations to steady flow is $\gamma = 0.021$, similar to the $\gamma = 0.53$ observed in vivo. For comparison, Fig. 6 shows the oscillatory velocity as measured in vivo. Its magnitude, phase, zero-crossing, and shape all resemble the prediction we can make by coupling the simulation results to realistic end boundary conditions.

4. Discussion

The central point of the Kedarasetti et al. study (24), as stated in its title, was to disprove the perivascular pumping hypothesis, particularly as supported by the experimental evidence of Mestre, Tifhof, et al. (12). To do so, those authors performed a series of simulations, finding disagreement with the in vivo observations and going on to conclude that perivascular pumping could not possibly drive the flows observed in vivo. However, those authors failed to couple their simulations to realistic end boundary conditions, and therefore did not represent the physiological system realistically. When we couple their results to realistic end boundary conditions, we find that their simulations of flow driven by perivascular pumping — and only perivascular pumping — closely match the flows observed in vivo by Mestre, Tithof, et al. Moreover, coupling two prior theoretical predictions (14, 21) to realistic boundary conditions likewise produces flows that closely match the in vivo observations. That broad agreement among four independent studies provides perhaps the strongest evidence yet that perivascular pumping is indeed the primary driver of CSF flow in PVSs under physiological conditions.

Our quantitative results are summarized in Table 1. The velocity $\overline{u}$ is averaged over the channel, except in the case of the Kedarasetti predictions, where centerline velocity was given. Uncoupled, predictions from theory and simulation all produce mean speeds roughly similar to in vivo observations, phase shifts much larger than in vivo observations, and oscillation ratios much larger than in vivo observations. Coupling to

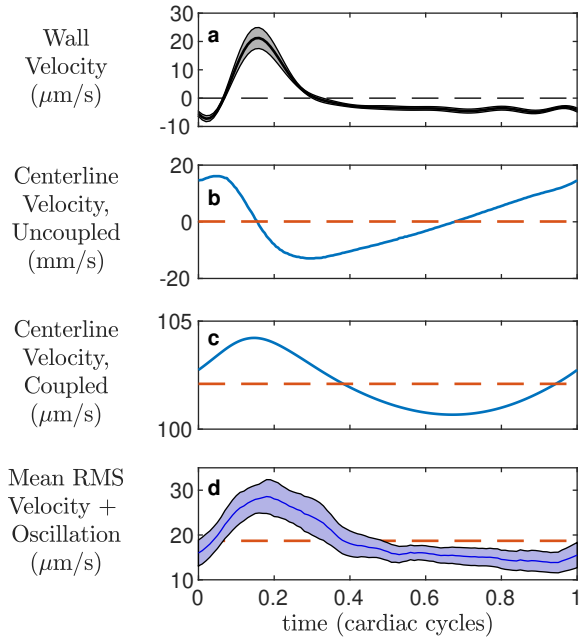

Fig. 6. Realistic boundary conditions bring good agreement between the fluid dynamical simulations of Kedarasetti et al. (24) and in vivo measurements. (a), In vivo measurements of artery wall velocity in the peri-arterial space surrounding the middle cerebral arteries of mice. The curve indicates the mean, and the shaded region indicates the standard error of the mean, over 7 mice. From (12). (b), Centerline fluid velocity in the simulations of (24), as driven by the wall velocity shown in (a). (c), Centerline fluid velocity after coupling to realistic boundary conditions, calculated numerically using Eq. 1, from the simulation results in (b). (d), In vivo measurements of oscillation of the root-mean-square velocity, in the same 7 experiments as in (a). The curve indicates the mean, and the shaded region indicates the standard error of the mean. Note that different units are used in panels (b) and (c). With realistic boundary conditions, the phase, relative oscillation amplitude, and oscillation shape are similar in simulations and in vivo observations.

realistic, lumped-parameter boundary conditions, based on our in vivo measurements, brings agreement in phase and oscillation ratio, in addition to mean speed.

One key implication of our findings is the general importance of using realistic boundary conditions when making predictions from theory or simulation. To the extent that the dynamics are linear, a lumped-parameter model can be coupled to theory or simulation a posteriori, as we have done here. However, in a case where nonlinear behaviors are appreciable, likely if the Womersley number or Reynolds number is large, accuracy requires including realistic boundary conditions in the theory or simulation itself. Lumped-parameter models are used routinely in simulations of cardiovascular flows, either as standalone models of the circulatory physiology, or coupled to hydrodynamic models as boundary conditions (44–46). Unfortunately, the $RC = 118.3$ s $\gg f^{-1}$ time constant we measure presents a particular challenge when simulating the CSF pathway. Transients decay on the RC timescale (see Eq. 3), so observing fully-developed dynamics will require simulating many cardiac cycles, at substantial and perhaps impractical computational expense.

Table 1. Summarized flow characteristics from theoretical predictions, simulation predictions, and in vivo observations.

	$\overline{u}$ (μm/s)	φ	γ
uncoupled Schley prediction	0.034	270°	22,200
uncoupled Wang prediction	10.13	270°	443
uncoupled Kedarasetti prediction	102.1	330°	290
coupled Schley prediction	0.034	0°	34.5
coupled Wang prediction	10.13	359.9°	0.069
coupled Kedarasetti prediction	102.1	356.4°	0.021
in vivo observations	18.7	353°	0.53

The lumped-parameter model used in this study was the simplest two-element Windkessel model; the model successfully captures the decay constant and phase relation in our study of perivascular flows. The three-element model, which adds a resistance (or impedance) in series with the RC circuit, captures high-frequency dynamics measured for aortic impedance in vivo, and hence is used widely in the cardiovascular community (47–49). Without measurements of glymphatic impedance over a wide frequency range, however, the need for a more complex model for perivascular flow is currently speculative, and may be the subject of future work.

Kedarasetti et al. (24) presented a third set of simulations in which the outer PVS wall was compliant, deforming in response to fluid pressure changes. As Sec. 1 describes, adding compliance to the system results in the dynamics of a lowpass filter, consistent with the fact that the oscillation ratio was much lower in that set of simulations. Also included was a prescribed pressure difference of order 0.01 mmHg, which drove mean flow through the low-resistance PVS. However, that boundary condition is again unrealistic, because the pressure at the ends of the PVS would be affected by coupling to the rest of the CSF pathway. Pial PVSs connect to a network of distal PVSs and interstitial space with much higher resistance, implying that much greater pressure differences would be required to drive flow.

We presented results of coupled flows in domains that are at least one wavelength in length. Asgari et al. (23) simulated a domain that is much shorter than the peristaltic wavelength, 0.1 to 0.2%, which is more physiologically realistic. Similar to others (14, 21, 24), they predict a flow rate with large $\gamma = 4,280$. However, their flow rate is nearly in phase with the wall velocity, in agreement with the in vivo measurements of Mestre, Tithof, et al. (12). The domain length likely results in a phase shift, which was also observed by Kedarasetti et al. in their simulation of a short domain (24). Coupling these subwavelength simulations to realistic resistance and compliance would likely match the γ of Mestre, Tithof, et al. (12), but the effect of realistic end boundary conditions on perivascular pumping in a domain shorter than a wavelength is unknown. We plan to study the effects of domain length in future work.

Our findings are subject to caveats. Most importantly, we have approximated the resistance R and compliance C of the rest of the CSF pathway — that is, all but the pial PVS — with values calculated from brain-wide measurements following cisterna magna injections. The pial perivascular space itself likely influences the dynamics we measured. Pathways parallel to the pial PVS, not connected to it, are also likely to affect R and C. Measuring those parameters more locally, in a way that distinguishes the resistance and compliance of the CSF pathway connected to a pial PVS from other CSF pathways, is an important topic for future work. That said, inaccuracies in R and C are unlikely to affect our key conclusions, since $RC \gg f^{-1}$ in any case. As mentioned above, the phase is less sensitive than the relative oscillation amplitude. We

expect that more accurate measurements of the rest of the CSF pathway would find resistance to be higher, not lower, because our brain-wide measurements are likely affected by shunt paths that allow CSF to exit the skull without passing through the brain parenchyma, as proposed recently (50, 51). Accuracy might also be improved by accounting for the internal resistance of the perivascular pump itself. However, when we estimated it using the known resistance of a concentric circular annulus of realistic size, our results changed little.

Our findings suggest that not only the mean flow $\overline{u}$, but also the phase φ and the normalized oscillation amplitude may vary with the state of wakefulness. Iontophoresis measurements have shown that the interstitial space in murine brain parenchyma increases 60% during sleep, and tracer measurements showed that mass transport through brain tissue increased by an order of magnitude (2). Thus it seems the mean flow increases during sleep. We hypothesize that the expanded interstitial space lowers the resistance R of the CSF pathway and therefore changes γ and φ as well, as expected from Eq. 1. We expect γ to be more sensitive to wakefulness state than φ, because the phase shift of a lowpass RC filter is nearly flat when $f \gg RC$. Future work might test this hypothesis. Other physiological changes that resize interstitial spaces, such as altering the osmotic potential (52), are likely to have similar effects.

An improved understanding of the mechanisms that drive CSF flow in the brain remains an important topic for future work. We have shown here that results from theory, simulation, and experiment are all consistent with perivascular pumping being a primary driver in physiological conditions. We hope our analysis will lead to more precise quantification of flows and driving mechanisms. Other mechanisms are known to dominate in pathological conditions like stroke (6) and to play a role in physiological conditions as well. Seeking flow and mechanisms at frequencies other than the heart rate, including the 0.05 Hz range of ventricular flow observed by (5), is a promising topic for future study. With realistic boundary conditions, first-principles simulations might be precise enough to quantify what fraction of the mean flow, if any, cannot be driven by arterial pulsations.

Materials and Methods

Animals and surgical preparation. We used 8- to 12-week-old male C57BL/6 mice acquired from Charles River Laboratories (Wilmington, MA, USA). In all experiments, animals were anesthetized with a combination of ketamine (100 mg/kg) and xylazine (10 mg/kg) administered intraperitoneally. Depth of anesthesia was determined by the pedal reflex test. The pedal reflex was tested every 5 to 10 min during the infusion experiment to ensure proper anesthesia throughout the study. If the mouse responded to toe pinch an additional 1/10 of the initial dosage was given and the infusion experiment was delayed until full unconsciousness was obtained. Body temperature was maintained at 37.5°C with a rectal probe-controlled heated platform (Harvard Apparatus). Anesthetized mice were fixed in a stereotaxic frame, and two cannulae were implanted into the right lateral ventricle (0.85 mm lateral, 2.10 mm ventral and 0.22 mm caudal to bregma) and the cisterna magna, as previously described (53). All experiments were approved by the University Committee on Animal Resources of the University of Rochester Medical Center (Protocol No. 2011-023), and an effort was made to minimize the number of animals used.

Evaluation of CSF dynamics. We measured hydraulic resistance and compliance using bolus injection, an approach introduced by Marmarou et al. (43). We injected fluid briefly and rapidly, measuring the resulting change in intracranial pressure (ICP), to estimate an impulse response, approximating the CSF pathway as a linear RC system. Using a computer-controlled syringe pump (Harvard Apparatus Pump 11 Elite), we injected $V = 5$ μL of artificial CSF (126 mM NaCl, 2.5 mM KCl, 1.25 mM NaH_2PO_4, 2 mM $MgSO_4$, 2 mM $CaCl_2$, 10 mM glucose, 26 mM $NaHCO_3$; pH 7.4 when gassed with 95% O_2 and 5% CO_2) at 1 μL/s into the right lateral ventricle. We monitored ICP via the cisterna magna cannulation connected to a transducer attached to a pressure monitor (BP-1, World Precision Instruments Inc., Sarasota, FL). We have verified that the results do not change appreciably if we instead inject into the cisterna magna and measure ICP in the ventricle. ECG and respiratory rate were also acquired using a small animal physiological monitoring device (Harvard Apparatus). All the signals were recorded at 1 kHz and digitized with a Digidata 1550A digitizer and AxoScope software (Axon Instruments).

We calculated the compliance C from the pressure-volume index (PVI): $C = \log_{10} e \cdot \mathrm{PVI}/P_0$, where e is the base of the natural logarithm. The PVI is defined as the volume of fluid required to cause a tenfold pressure increase during bolus injection:

$$\mathrm{PVI} = \frac{V}{\log_{10} \frac{P_{\max}}{P_0}}.$$

The resistance R can be estimated as

$$R = \frac{tP_0}{\mathrm{PVI} \log_{10} \frac{P(t)(P_{\max}-P_0)}{P_{\max}(P(t)-P_0)}}, \qquad [4]$$

where $P(t)$ is the pressure measured at time t. We expect R to be nearly constant, but to increase accuracy, we estimate R for each animal by averaging the results of Eq. 4 at five evenly-spaced times during the experiment.

Data is available from the authors upon reasonable request.

ACKNOWLEDGMENTS. This work was supported by the NIH National Institute of Aging (grant RF1AG057575) and by the U. S. Army Research Office (grant MURI W911NF1910280). The authors are grateful for fruitful conversations with J. H. Thomas and J. Tithof, and for expert illustration by D. Xue.

1. Iliff JJ, et al. (2012) A Paravascular Pathway Facilitates CSF Flow Through the Brain Parenchyma and the Clearance of Interstitial Solutes, Including Amyloid . *Science Translational Medicine* 4(147):147ra111–147ra111.
2. Xie L, et al. (2013) Sleep Drives Metabolite Clearance from the Adult Brain. *Science* 342(6156):373–377.
3. Ratner V, et al. (2017) Cerebrospinal and interstitial fluid transport via the glymphatic pathway modeled by optimal mass transport. *NeuroImage* 152:530–537.
4. Koundal S, et al. (2020) Optimal Mass Transport with Lagrangian Workflow Reveals Advective and Diffusion Driven Solute Transport in the Glymphatic System. *Sci. Rep.* pp. 1–18.
5. Fultz NE, et al. (2019) Coupled electrophysiological, hemodynamic, and cerebrospinal fluid oscillations in human sleep. *Science*.
6. Mestre H, et al. (2020) Cerebrospinal fluid influx drives acute ischemic tissue swelling. *Science* 9:eaax7171–24.
7. Louveau A, et al. (2015) Structural and functional features of central nervous system lymphatic vessels. *Nature* 523(7560):337–341.
8. Mesquita S, et al. (2018) Functional aspects of meningeal lymphatics in ageing and Alzheimer's disease. *Nature* pp. 1–32.
9. Ahn JH, et al. (2019) Meningeal lymphatic vessels at the skull base drain cerebrospinal fluid. *Nature* pp. 1–29.
10. Rennels ML, Gregory TF, Blaumanis OR, Fujimoto K, Grady PA (1985) Evidence for a 'paravascular'fluid circulation in the mammalian central nervous system, provided by the rapid distribution of tracer protein throughout the brain from the subarachnoid space. *Brain Research* 326(1):47–63.
11. Rennels M, Blaumanis O, Grady P (1990) Rapid solute transport throughout the brain via paravascular fluid pathways. *Advances in Neurology* 52:431–439.
12. Mestre H, et al. (2018) Flow of cerebrospinal fluid is driven by arterial pulsations and is reduced in hypertension. *Nat. Commun.* 9(1):4878.
13. Bedussi B, Almasian M, de Vos J, VanBavel E, Bakker EN (2017) Paravascular spaces at the brain surface: Low resistance pathways for cerebrospinal fluid flow. *J Cerebr Blood F Met* 38(4):719–726.
14. Schley D, Carare-Nnadi R, Please CP, Perry VH, Weller RO (2006) Mechanisms to explain the reverse perivascular transport of solutes out of the brain. *J. Theor. Biol.* 238(4):962–974.
15. Bakker ENTP, et al. (2017) Lymphatic Clearance of the Brain: Perivascular, Paravascular and Significance for Neurodegenerative Diseases. *Cellular and Molecular Neurobiology* 36(2):181–194.
16. Mestre H, Mori Y, Nedergaard M (2020) The Brain's Glymphatic System: Current Controversies. *Trends in Neurosciences*.
17. Ray LA, Heys JJ (2019) Fluid Flow and Mass Transport in Brain Tissue. *Fluids* 4(4):196–33.

18. Hadaczek P, et al. (2006) The "Perivascular Pump" Driven by Arterial Pulsation Is a Powerful Mechanism for the Distribution of Therapeutic Molecules within the Brain. *Mol. Ther.* 14(1):69–78.
19. Iliff JJ, et al. (2013) Cerebral Arterial Pulsation Drives Paravascular CSF-Interstitial Fluid Exchange in the Murine Brain. *J Neurosci* 33(46):18190–18199.
20. Jaffrin MY, Shapiro AH (1971) Peristaltic pumping. *Annu. Rev. Fluid Mech.* 3:13–37.
21. Wang P, Olbricht WL (2011) Fluid mechanics in the perivascular space. *J. Theor. Biol.* 274(1):52–57.
22. Bilston LE, Fletcher DF, Brodbelt AR, Stoodley MA (2003) Arterial Pulsation-driven Cerebrospinal Fluid Flow in the Perivascular Space: A Computational Model. *Computer Methods in Biomechanics and Biomedical Engineering* 6(4):235–241.
23. Asgari M, de Zélicourt D, Kurtcuoglu V (2016) Glymphatic solute transport does not require bulk flow. *Sci. Rep.* pp. 1–11.
24. Kedarasetti RT, Drew PJ, Costanzo F (2020) Arterial pulsations drive oscillatory flow of CSF but not directional pumping. *Sci. Rep.* pp. 1–12.
25. Rey J, Sarntinoranont M (2018) Pulsatile flow drivers in brain parenchyma and perivascular spaces: a resistance network model study. *Fluids and Barriers of the CNS* 15(1):20.
26. Kedarasetti R, et al. (2019) Functional hyperemia drives fluid exchange in the paravascular space. *bioRxiv* p. 838813.
27. Thomas JH (2019) Fluid dynamics of cerebrospinal fluid flow in perivascular spaces. *J. R. Soc. Interface* 16(159):20190572–11.
28. Tithof J, Kelley DH, Mestre H, Nedergaard M, Thomas JH (2019) Hydraulic resistance of periarterial spaces in the brain. *Fluids and Barriers of the CNS* 16(1):19.
29. Diem AK, et al. (2017) Arterial Pulsations cannot Drive Intramural Periarterial Drainage: Significance for Aβ Drainage. *Front. Neurosci.* 11:353–9.
30. Smith AJ, Yao X, Dix JA, Jin BJ, Verkman AS (2017) Test of the'glymphatic'hypothesis demonstrates diffusive and aquaporin-4-independent solute transport in rodent brain parenchyma. *Elife* 6:e27679.
31. Faghih MM, Sharp MK (2018) Is bulk flow plausible in perivascular, paravascular and paravenous channels? *Fluids and Barriers of the CNS* pp. 1–10.
32. Croci M, Vinje V, Rognes ME (2019) Uncertainty quantification of parenchymal tracer distribution using random diffusion and convective velocity fields. *Fluids and Barriers of the CNS* pp. 1–21.
33. van Veluw SJ, et al. (2019) Vasomotion as a Driving Force for Paravascular Clearance in the Awake Mouse Brain. *Neuron* pp. 1–31.
34. Bakker ENTP, Naessens DMP, VanBavel E (2019) Paravascular spaces: entry to or exit from the brain? *Exp Physiol* 104(7):1013–1017.
35. Jones H (1985) Cerebrospinal fluid pressure and resistance to absorption during development in normal and hydrocephalic mutant mice. *Experimental neurology* 90(1):162–172.
36. Kosteljanetz M (1985) Resistance to outflow of cerebrospinal fluid determined by bolus injection technique and constant rate steady state infusion in humans. *Neurosurgery* 16(3):336–340.
37. Eklund A, et al. (2007) Assessment of cerebrospinal fluid outflow resistance. *Medical & biological engineering & computing* 45(8):719–735.
38. Oshio K, Watanabe H, Song Y, Verkman A, Manley GT (2005) Reduced cerebrospinal fluid production and intracranial pressure in mice lacking choroid plexus water channel Aquaporin-1. *The FASEB journal* 19(1):76–78.
39. Yang L, et al. (2013) Evaluating glymphatic pathway function utilizing clinically relevant intrathecal infusion of CSF tracer. *Journal of translational medicine* 11(1):107.
40. Moazen M, et al. (2016) Intracranial pressure changes during mouse development. *Journal of biomechanics* 49(1):123–126.
41. Wang X, et al. (2020) An ocular glymphatic clearance system removes β-amyloid from the rodent eye. *Science Translational Medicine* 12(536).
42. Papadopoulos MC, Manley GT, Krishna S, Verkman A (2004) Aquaporin-4 facilitates reabsorption of excess fluid in vasogenic brain edema. *The FASEB journal* 18(11):1291–1293.
43. Marmarou A, Shulman K, Rosende RM (1978) A nonlinear analysis of the cerebrospinal fluid system and intracranial pressure dynamics. *J Neurosurg* 48(3):332–344.
44. Stergiopulos N, Young D, Rogge T (1992) Computer simulation of arterial flow with applications to arterial and aortic stenoses. *Journal of Biomechanics* 25(12):1477 – 1488.
45. Vignon-Clementel IE, Figueroa] CA, Jansen KE, Taylor CA (2006) Outflow boundary conditions for three-dimensional finite element modeling of blood flow and pressure in arteries. *Computer Methods in Applied Mechanics and Engineering* 195(29):3776 – 3796. Absorbing Boundary Conditions.
46. Tran JS, Schiavazzi DE, Ramachandra AB, Kahn AM, Marsden AL (2017) Automated tuning for parameter identification and uncertainty quantification in multi-scale coronary simulations. *Computers & fluids* 142:128–138.
47. Burkhoff D, Alexander Jr J, Schipke J (1988) Assessment of windkessel as a model of aortic input impedance. *American Journal of Physiology-Heart and Circulatory Physiology* 255(4):H742–H753.
48. Westerhof N, Bosman F, De Vries CJ, Noordergraaf A (1969) Analog studies of the human systemic arterial tree. *Journal of biomechanics* 2(2):121–143.
49. Westerhof N, Elzinga G, Sipkema P (1971) An artificial arterial system for pumping hearts. *Journal of applied physiology* 31(5):776–781.
50. Ma Q, Decker Y, Müller A, Ineichen BV, Proulx ST (2019) Clearance of cerebrospinal fluid from the sacral spine through lymphatic vessels. *J Exp Med* 82:jem.20190351–11.
51. Vinje V, Eklund A, Mardal KA, Rognes ME, Støverud KH (2020) Intracranial pressure elevation alters CSF clearance pathways. *Fluids and Barriers of the CNS* pp. 1–19.
52. Plog BA, et al. (2018) Transcranial optical imaging reveals a pathway for optimizing the delivery of immunotherapeutics to the brain. *JCI Insight* 3(20):1188–16.
53. Xavier AL, et al. (2018) Cannula implantation into the cisterna magna of rodents. *JoVE (Journal of Visualized Experiments)* (135):e57378.